Front. Mech. Eng. 2022, 17(4): 52
https://doi.org/10.1007/s11465-022-0708-0

RESEARCH ARTICLE

M-LFM: a multi-level fusion modeling method for shape–performance integrated digital twin of complex structure

Xiwang HE[a], Xiaonan LAI[a], Liangliang YANG[a], Fan ZHANG[b], Dongcai ZHOU[b], Xueguan SONG (✉)[a], Wei SUN[a]

[a] *School of Mechanical Engineering, Dalian University of Technology, Dalian 116024, China*
[b] *Sany Marine Heavy Industry Co., Ltd., Zhuhai 519090, China*
✉ *Corresponding author. E-mail: sxg@dlut.edu.cn (Xueguan SONG)*

ABSTRACT As a virtual representation of a specific physical asset, the digital twin has great potential for realizing the life cycle maintenance management of a dynamic system. Nevertheless, the dynamic stress concentration is generated since the state of the dynamic system changes over time. This generation of dynamic stress concentration has hindered the exploitation of the digital twin to reflect the dynamic behaviors of systems in practical engineering applications. In this context, this paper is interested in achieving real-time performance prediction of dynamic systems by developing a new digital twin framework that includes simulation data, measuring data, multi-level fusion modeling (M-LFM), visualization techniques, and fatigue analysis. To leverage its capacity, the M-LFM method combines the advantages of different surrogate models and integrates simulation and measured data, which can improve the prediction accuracy of dynamic stress concentration. A telescopic boom crane is used as an example to verify the proposed framework for stress prediction and fatigue analysis of the complex dynamic system. The results show that the M-LFM method has better performance in the computational efficiency and calculation accuracy of the stress prediction compared with the polynomial response surface method and the kriging method. In other words, the proposed framework can leverage the advantages of digital twins in a dynamic system: damage monitoring, safety assessment, and other aspects and then promote the development of digital twins in industrial fields.

KEYWORDS shape–performance integrated digital twin (SPI-DT), multi-level fusion modeling (M-LFM), surrogate model, telescopic boom crane, data fusion

1 Introduction

Since Germany proposed Industry 4.0 in 2013, the Fourth Industrial Revolution driven by technologies, such as the Internet of Things, Big Data, robotics, and artificial intelligence, has been sweeping the world unprecedentedly [1]. This revolution has given birth to emerging industries, such as data analysis, cloud computing, and artificial intelligence, and other industries, such as software and robotics, and the Internet, have also entered a stage of rapid development [2]. In such a context, the digital twin is fast evolving for engineering systems since it is possible to establish a real-time connection between the physical world and the virtual world. More specifically, structural dynamic problems operating in harsh environments have attracted more research interest, such as dynamic reliability analysis of tower cranes and helicopter dynamic systems [3–5]. The research on digital twins can be traced back to Professor Michael Grieves's product lifecycle management model at the University of Michigan in 2003 [6]. However, the birth of the concept of digital twins did not attract enough attention until the term "digital twins" appeared in the National Aeronautics and Space Administration's comprehensive technology roadmap [7,8]. Virtual models can replace physical components with the development of simulation technology, which provides the possibility of constructing a digital twin model in the life cycle of a physical system [9].

The digital twin model can be used to simulate and reflect the real-time behavior of the physical system under operating conditions in the life cycle [10,11]. The process of building a digital twin model consists of many parts, such as geometric model construction, mechanism

Received January 20, 2022; accepted May 17, 2022

model construction, data model construction, and data transmission. All of these parts can affect the accuracy and efficiency of digital twins in practical engineering applications. Data model construction is the most crucial for the building process of digital twins; it influences the reliability and efficiency of the outputs. The combination of the physical model and the dynamic data model was considered a reasonable solution to enhance the efficiency of digital twins. Ritto and Rochinha [12] proposed a framework that combines physics-based models and machine learning models to implement real-time engineering decisions on damaged structures, which ensures the interpretability and real-time behavior of digital twins. Lai et al. [13] proposed a shape–performance integrated digital twin (SPI-DT) framework based on multiple models and introduced the digital twin design process for the structure of complex heavy equipment, with a telescopic boom crane as an example. Kapteyn et al. [14] developed a digital twin of a fixed-wing unmanned aerial vehicle by establishing a library of component-based reduced-order models and using optimal trees to invoke physics-based reduced models in the model library. Luo et al. [15] proposed a data-based hybrid method to realize the predictive maintenance of computerized numerical control machine tools. The results showed that the proposed method demonstrated better predictive performance compared with a single method. However, in the aforementioned studies, the digital twin model is built using simulation data; therefore, the accuracy of the model depends on the simulation model. From the viewpoint of the reliability of digital twins, there is much research focused on the combination of the simulation and measured data to realize the application of the digital twin for the complex heavy equipment. Wang et al. [16] established a multi-fidelity surrogate model to realize the fusion of measured and simulation data, which further improved the prediction accuracy of the digital twin model. Kontaxoglou et al. [17] proposed a multi-fidelity framework combined with sparse telemetry data to treat the simulation of a small satellite and proved the feasibility of the framework. Chetan et al. [18] introduced a multi-fidelity digital twin model to conduct performance maintenance of wind turbine blades, which further provided a clue to developing the multi-fidelity digital twin in structural monitoring. They help improve the credibility of digital twins, but this approach will increasingly affect the computational effort.

More importantly, engineers often pay the most attention to the vulnerable area of the structure, i.e., the area where the structural stress is concentrated for practical engineering problems. For example, because the weld is more prone to stress concentration, the position of the weld is more prone to failure than the base metal [19]. For large and complex mechanical structures, fatigue failure can be avoided in advance by accurately predicting the stress at the location where the structure is prone to damage [20]. However, because of the complex stress changes in the dynamic system, the existing modeling methods cannot meet the prediction accuracy of the vulnerable area of the structure. Therefore, how to improve the stress prediction accuracy of key locations of large and complex mechanical structures is a crucial issue in realizing structural life monitoring. The combination of hybrid modeling methods [21] and multi-fidelity modeling methods [22] provides the possibility of solving the above problems to improve the prediction accuracy of the structural stress concentration area of the dynamic system while balancing the requirements of digital twins for high precision and instantaneity.

In such a context, the multi-level fusion modeling (M-LFM) method was proposed to be integrated into the SPI-DT framework. The M-LFM method not only considers the influence of both simulation and measured data on the model accuracy but also combines the polynomial response surface (PRS) method and the kriging (KRG) method to solve the problem of model efficiency. The main advantage of the M-LFM method is in using both measured and simulation data to establish a regional compensation model for the dynamic stress concentration area, which can more accurately describe the mechanical behavior of complex structures. Taking the telescopic boom crane as an example, the feasibility of the framework is verified by establishing a digital twin of the telescopic boom to make real-time performance predictions. Note that the method can be seen as a general paradigm for combining test and simulation data in a digital twin.

The remainder of this paper is organized as follows. Section 2 presents the introduction of the PRS and KRG models. Section 3 gives the details of the proposed framework and the M-LFM method. Section 4 gives the verification of the feasibility of the proposed framework, using a telescopic boom crane case as an example. Section 5 gives conclusions and future work.

2 Research background

The surrogate model is used to determine the mathematical relationship between input and output using limited sample information. This model has been widely used in the design and optimization of structural and multidisciplinary complex equipment [23]. Given that the digital twins also need a data-driven model to realize the real-time calculation of the physical model, there is a compelling reason for establishing the surrogate model: To establish an effective means to realize digital twins [24]. Popular surrogate models applicable in the structural optimization field include PRS, the KRG model, radial basis function, support vector regression, and moving least squares.

2.1 Polynomial response surface method

The PRS method, which is also called the polynomial regression analysis method, is an important type of regression analysis. The PRS method is based on a set of observation data, through research to determine the quantitative relationship between the target output and multiple independent variables [25]. For any observation point, there is a corresponding linear expression:

$$\boldsymbol{Y} = \boldsymbol{X}\boldsymbol{\alpha} + \boldsymbol{\varepsilon}, \tag{1}$$

where $\boldsymbol{X}$ is the input vector, $\boldsymbol{Y}$ is the output vector, $\boldsymbol{\alpha}$ is the vector of unknown coefficients, $\boldsymbol{\varepsilon}$ is the vector of error function, and its expectation and variance can be respectively expressed as zero and σ^2.

In the field of mechanical design optimization, the first- or second-order PRS is used to approximate the relationship between the input and output of the design variables using the training data in practical applications. The unknown coefficients are calculated and solved based on the least square method that is solved by minimizing the variance of unbiased estimates of unknown coefficients based on the Gauss–Markov theorem. Assuming the $\hat{y}$ is the predicted value of the target output, which is calculated by the following formula:

$$\hat{y}(x) = \sum_{i=1}^{m} \alpha_i \psi_i(x), \tag{2}$$

where x is the input variable, $\psi_i(x)$ is correlated with the physical properties of problem itself, m is the number of input variables, and α_i is the unknown weight coefficient. The PRS method can fit functions with larger curvatures by providing an approximate relationship between the dependent variable and the independent variables. The prediction calculation efficiency is higher because the model parameters are less, which makes the PRS method widely used in the field of structural optimization. Nevertheless, the disadvantage of using the PRS method is that it is difficult to accurately predict the functional relationship with a high degree of nonlinearity.

2.2 Kriging model

The KRG model was summarized by a French mathematician Georges Matheron in 1962 based on the South African geologist Danie G. Krige's doctoral dissertation on geostatistics on gold mining prediction [26]. The KRG model is an optimized interpolation algorithm that simulates interpolation through a Gaussian process controlled by covariance to generate a continuous function. This method considers not only the influence of the distance relationship between the sampling points on the output change but also the influence of the position relationship and the spatial distribution between the sampling points on the overall output. The expression consists of two parts as follows:

$$\boldsymbol{Y} = \sum_{i=1}^{m} \beta_i f_i(\boldsymbol{X}) + z(\boldsymbol{X}), \tag{3}$$

where $f_i(\boldsymbol{X})$ represents an unknown approximate function, β_i represents an unknown weighted coefficient, and $z(\boldsymbol{X})$ represents an error function of KRG model with mean zero and variance σ^2. The covariance matrix of $z(\boldsymbol{X})$ is given as follows:

$$\operatorname{cov}\left[z(x_i), z(x_j)\right] = \sigma^2 \boldsymbol{R}\left[R(x_i, x_j)\right], \tag{4}$$

where R is the relationship function and generally is a Gaussian function, and $\boldsymbol{R}$ is the relationship matrix whose elements are the value of relationship function. Once the relationship function is determined, the predicted value of the target output can be expressed as follows:

$$\hat{y}(x) = \hat{\beta} + \boldsymbol{r}^{\mathrm{T}}(x)\boldsymbol{R}^{-1}\left(\boldsymbol{y}_{\mathrm{s}} - \hat{\beta}\boldsymbol{H}\right), \tag{5}$$

where $\boldsymbol{H} = [1 \quad 1 \quad \cdots \quad 1]^{\mathrm{T}}$ is a vector whose elements are ones, $\boldsymbol{r}$ is a related vector between the unknown predicted point and the trained point, and $\boldsymbol{y}_{\mathrm{s}}$ is the true response value at samples. $\hat{\beta}$ is a maximum likelihood estimation value of hyper-parameter, which can be expressed as

$$\hat{\beta} = (\boldsymbol{H}^{\mathrm{T}}\boldsymbol{R}^{-1}\boldsymbol{H})^{-1}\boldsymbol{H}^{\mathrm{T}}\boldsymbol{R}^{-1}\boldsymbol{y}_{\mathrm{s}}. \tag{6}$$

The advantage of the KRG method is that it generates an interpolated spatial model and an uncertainty estimate for each predicted point in the model. Additionally, compared with the PRS method, the KRG method makes observations based on a sample data point rather than on a prehypothesized model. This means that the KRG method may be difficult to meet real-time requirements for the performance prediction of large and complex structures since it has a high complexity [27].

3 SPI-DT framework based on the M-LFM method

3.1 Proposed framework

The digital twin model was originally considered to be divided into three parts: 1) physical entity, 2) virtual entity, and 3) connections [28]. Based on this classification, Tao et al. [29] proposed a digital twin five-dimensional (5D) model (the physical entity, the virtual entity, connections, twins data, and services) to satisfy new demands in the application of digital twins. Therefore, the digital twin not only should meet the real-time connection between the physical space and the virtual space but, more importantly, it should consider its applications and services in the physical world. For the SPI-DT framework, "shape" means the physical appearance of a product in the digital twin, including the information about dimension and geometry, such as the size, volume, and texture. The shape of a product can be

obtained by scanning or 3D modeling. “Performance” means the performance of a product. The performance of a product can be obtained via analytical method, numerical simulation, or experimental measurements, such as stress or strain of a structure or product, the temperature distribution of battery packs, and the remaining useful life (RUL) of a product. “Shape-performance” means that the digital twin can display the physical appearance and performance simultaneously. For example, the digital twin of the telescopic boom crane can display not only the physical appearance of the boom but also the stress distribution of the members in real-time.

Based on the SPI-DT framework, more attention should be given to the stress in the area where the structure is prone to damage, which can help to avoid the loss of economic benefits caused by structural failure. Meanwhile, the stress in other areas must also be monitored by a cheap model for the structure in real-time. However, the degree of nonlinearity in the prediction of each area is different since the complicated loading conditions of complex large-scale mechanical structures, which cause stress prediction relying solely on the PRS method or the KRG method, cannot meet the real-time and high-precision requirements of the digital twin. Accordingly, an SPI-DT framework based on the M-LFM method was proposed for the structural fatigue area to reduce the time complexity and improve the predicted accuracy of the predicted model, as shown in Fig. 1.

The proposed framework comprises three parts, namely, data collection, model construction, and visualization and interaction. The data collection part involves the experimental test and simulation calculation of the structure, which are used to train the predicted model and determine the parameters of the model. The model construction part involves the proposed M-LFM method that is composed of the prediction model of the entire region based on the PRS model and the stress concentration area based on the KRG model, which allows the prediction model’s accuracy to be improved by combining the spatial coordinates to dynamically adjust the stress in the area around the stress concentration. The last part is the visualization and interaction part, which is composed of the physical space and virtual space, which are used to read real-time dynamic sensors’ data and achieve visual feedback of performance predictions. In the proposed framework, data collection and model construction are conducted in the offline stage to realize the data fusion and model training, respectively, which have been stored in the virtual space. The visualization and interaction are performed in the online stage to read the dynamic sensors’ data and input it into the trained prediction model to achieve performance prediction in real time. Then, the physical model is visualized in the virtual space based on the geometric and performance data of the physical model and gives feedback to the engineers in real time.

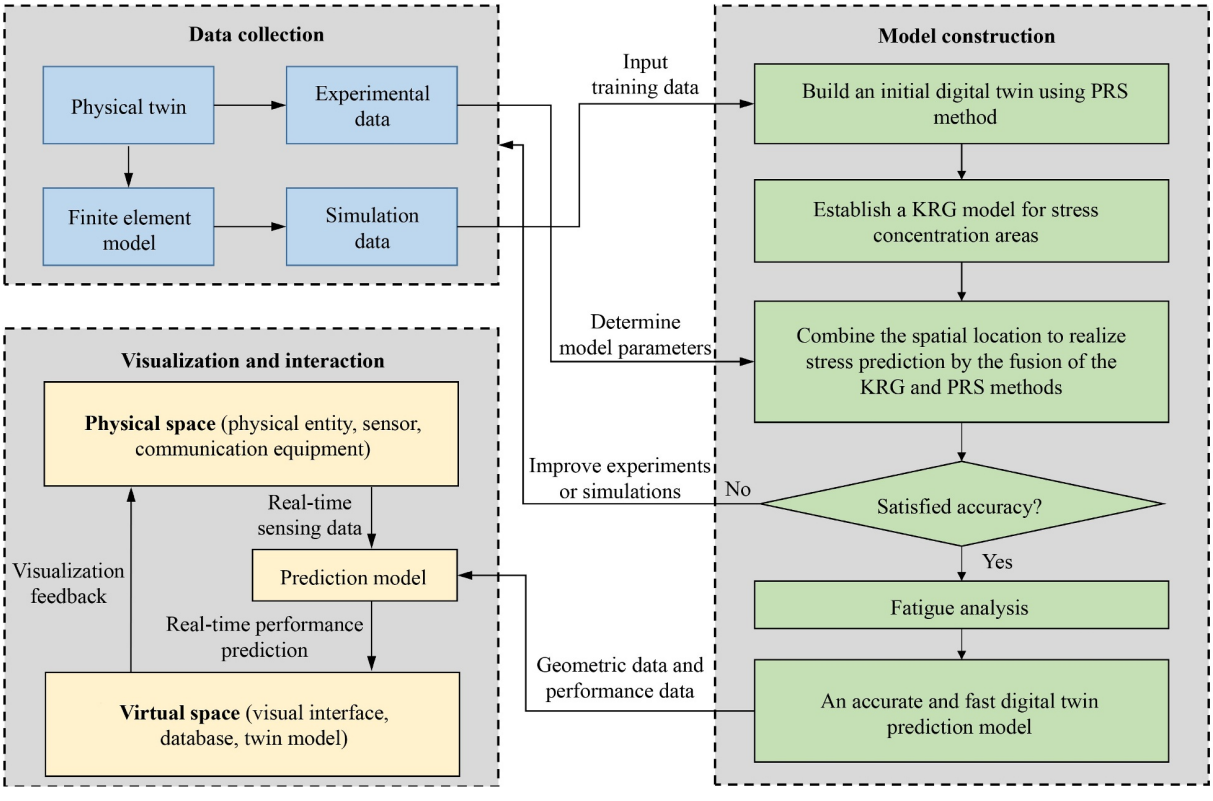

Fig. 1 A credible and fast digital twin framework based on the multi-level fusion modeling method.

3.2 Multi-level fusion modeling method

For actual structural analysis problems, the structure should be discretized to perform dynamic analysis, simulation, and design of the structure, which can be expressed as the following:

$$\boldsymbol{\sigma} = f(\boldsymbol{X}), \tag{7}$$

where $\boldsymbol{\sigma} = [\sigma_1, \sigma_2, ..., \sigma_n]^{\mathrm{T}}$ represents the performance vector, n is the number of performance data, and $\boldsymbol{X} = [\boldsymbol{x}_1, \boldsymbol{x}_2, ..., \boldsymbol{x}_n]^{\mathrm{T}}_{n\times m}$ is the input vector. First, after the discretization of the structure, the PRS model is used to establish a low-fidelity model of stress prediction. Second, the training point is used to discretize the dynamic process into multiple stress values under the static process:

$$\boldsymbol{Y}_{\mathrm{PRS}} = \boldsymbol{X}\boldsymbol{\alpha} + \boldsymbol{\varepsilon}, \tag{8}$$

where $\boldsymbol{Y}_{\mathrm{PRS}} = [\hat{y}_1^{\mathrm{PRS}}, \hat{y}_2^{\mathrm{PRS}}, ..., \hat{y}_n^{\mathrm{PRS}}]^{\mathrm{T}}$ are the predicted vector of the PRS model. Because of the dynamic change in the contact position for mechanical structures that move between components, the stress concentration area will also change, resulting in a higher degree of nonlinearity in the stress concentration area. Hence, the KRG model is used to predict the high nonlinearity stress concentration area and improve the stress prediction accuracy of the area around the compensation point. Assuming that there are N compensation areas in a certain motion state, the prediction equation considering the motion characteristics of the structure is as follows:

$$\boldsymbol{Y}_{\mathrm{KRG}} = \hat{\beta} + \boldsymbol{r}^{\mathrm{T}}(\boldsymbol{X})\boldsymbol{R}^{-1}\left(\boldsymbol{y}_{\mathrm{s}} - \hat{\beta}\boldsymbol{H}\right), \tag{9}$$

where $\boldsymbol{Y}_{\mathrm{KRG}} = [\hat{y}_1^{\mathrm{KRG}}, \hat{y}_2^{\mathrm{KRG}}, ..., \hat{y}_N^{\mathrm{KRG}}]^{\mathrm{T}}$ are the predicted vector of the KRG model. Although the KRG method has higher nonlinear data processing capabilities, establishing an effective stress compensation function at the area surrounding the compensation point is crucial to improving the stress prediction accuracy. First, the scale factor between the prediction results of the KRG model and the PRS model in the dynamic stress compensation area is determined as follows:

$$b = \frac{\hat{y}_C^{\mathrm{PRS}} - \hat{y}_C^{\mathrm{KRG}}}{\hat{y}_C^{\mathrm{PRS}}}, \tag{10}$$

where $\hat{y}_C^{\mathrm{PRS}}$ and $\hat{y}_C^{\mathrm{KRG}}$ represent the predicted value of the PRS model and the KRG model at the compensation point C, respectively, and b is the scale factor. Then, the Euclidean distance ρ_i between the compensation point and the surrounding points is introduced to determine the scope of influence for establishing the stress compensation function:

$$\rho_i = \sqrt{(u_i - u_C)^2 + (v_i - v_C)^2 + (w_i - w_C)^2},\ i = 1, 2, ..., n, \tag{11}$$

where u_i, v_i, and w_i represent the space coordinates in the ith point, and u_C, v_C, and w_C represent the space coordinates in the compensation point C. The normal Euclidean distance is denoted as $\rho_i^{\mathrm{nor}} = \dfrac{\rho_i - \rho_{\min}}{\rho_{\max} - \rho_{\min}}$ where $\rho_{\min}$ and $\rho_{\max}$ is the minimum and maximum values of the Euclidean distance set. A crucial problem is that the position of the compensation point may be constantly dynamic, changing with each component move. In this scheme, the Gaussian function is introduced as the compensation function to determine the compensation factor of the surrounding points, which can reflect the movement characteristics between structures based on the change in Euclidean distance.

$$Cf_i = \frac{1}{\sqrt{2\pi\delta^2}} \cdot \exp\left(-\frac{(\rho_i^{\mathrm{nor}} - \mu)^2}{2\delta^2}\right),\ i = 1, 2, ..., n, \tag{12}$$

where Cf_i is compensation factor of the influence domain, δ represents the parameter of the influence domain, and μ is the coefficient of deviation of the compensation point. Afterward, the obtained compensation factor should be normalized:

$$Cf_i^{\mathrm{nor}} = \frac{Cf_i - Cf_{\min}}{Cf_{\max} - Cf_{\min}}, \tag{13}$$

where Cf_i^{nor} is normalized compensation factor, and $Cf_{\min}$ and $Cf_{\max}$ are the minimum and maximum values of the compensation factor set. Finally, the predicted value of stress at any point after compensation can be obtained as follows:

$$\hat{y}_i = \hat{y}_i^{\mathrm{PRS}} + \hat{y}_i^{\mathrm{PRS}} abCf_i^{\mathrm{nor}} = \hat{y}_i^{\mathrm{PRS}}(1 + abCf_i^{\mathrm{nor}}),\ i = 1, 2, ..., n, \tag{14}$$

where $(\hat{y}_1, \hat{y}_2, ..., \hat{y}_n) \in \mathrm{R}^n$ are predicted value at sample points, and a is the unknown coefficient used to change the result size of the predicted model. In the design process of the proposed method, three unknown parameters, the ratio a, the deviation coefficient μ, and the influence domain parameters δ, should be determined. Assuming that the simulation model is consistent with the real-world stress distribution in the whole structure, the training data can be used to determine the parameters μ and δ. Since the PRS model is a polynomial fitting method, there is a certain error at the training point. The optimization of parameters is performed by minimizing the error e between the training value and the predicted value at the training point in the design space to determine the optimal μ and δ:

$$\begin{cases} e = \min\left(\sum_{i=1}^{n}\left(y_i^{\mathrm{train}} - \hat{y}_i\right)^2\right), \\ \text{s.t.} \quad \delta_{\mathrm{l}} < \delta_i < \delta_{\mathrm{u}},\ \mu_{\mathrm{l}} < \mu_i < \mu_{\mathrm{u}}, \end{cases} \tag{15}$$

where y_i^{train} is response value in the ith training point, δ_{l} and δ_{u} indicate the lower and upper bounds of the parameter δ, respectively, and μ_{l} and μ_{u} represent the lower and upper bounds of the parameter μ, respectively. The optimal parameters $\boldsymbol{\delta}_{\mathrm{opt}} = [\delta_1, \delta_2, ..., \delta_m]^{\mathrm{T}}$ and $\boldsymbol{\mu}_{\mathrm{opt}} = [\mu_1, \mu_2, ..., \mu_m]^{\mathrm{T}}$ at each training point are determined

through optimization. The value of the proportional a can be determined by the measured data to make the predicted result more suitable for the actual measurement result. Assuming the measured data is $\boldsymbol{T}^{\text{test}}$ and predicted data of PRS model is $\hat{\boldsymbol{y}}^{\text{PRS}}$, the error ε_i at the measuring point can be expressed as the following:

$$\varepsilon_i = (T_i^{\text{test}} - \hat{y}_i)^2,\ i = 1,2,...,k. \tag{16}$$

By constructing and minimizing the cost function L to find the parameter value a, we have

$$\begin{aligned} L &= \sum_{i=1}^{k} \varepsilon_i = \sum_{i=1}^{k} (T_i^{\text{test}} - \hat{y}_i)^2 \\ &= \sum_{i=1}^{k} (T_i^{\text{test}} - (1 + abCf_i^{\text{nor}})\hat{y}_i^{\text{PRS}})^2, \end{aligned} \tag{17}$$

where b and Cf_i^{nor} are constant, and k is the number of measured data. The equation obtained by differentiating Eq. (17) with respect to a can be expressed as the following:

$$\frac{\partial L}{\partial a} = 2b\boldsymbol{Cf}_{\text{nor}} \cdot \hat{\boldsymbol{y}}^{\text{PRS}} \cdot \left(\boldsymbol{T}^{\text{test}} - (1 + ab\boldsymbol{Cf}_{\text{nor}}) \cdot \hat{\boldsymbol{y}}^{\text{PRS}}\right), \tag{18}$$

where $\boldsymbol{Cf}_{\text{nor}}$ is the compensation factor set. Make $\frac{\partial L}{\partial a} = 0$. Then, $\boldsymbol{a}_{\text{opt}}$ can be expressed as the following:

$$\boldsymbol{a}_{\text{opt}} = \frac{\boldsymbol{T}^{\text{test}} - \hat{\boldsymbol{y}}^{\text{PRS}}}{b\boldsymbol{Cf}_{\text{nor}} \cdot \hat{\boldsymbol{y}}^{\text{PRS}}}. \tag{19}$$

Therefore, the optimal parameters $\boldsymbol{a}_{\text{opt}} = [a_1, a_2, ..., a_k]^{\text{T}}$ can be obtained based on the measured data and predicted data. The optimal parameters at different compensation points are different due to the mutual movement of the components, and the relationship between external sensor data and optimization parameters should also be established. The prediction model of the parameters under different sensors data is established based on the PRS model:

$$\hat{\delta} = \sum_{i=1}^{m} \alpha_i^{\delta} \psi_i^{\delta}(x), \tag{20}$$

$$\hat{\mu} = \sum_{i=1}^{m} \alpha_i^{u} \psi_i^{u}(x), \tag{21}$$

$$\hat{a} = \sum_{i=1}^{k} \alpha_i^{a} \psi_i^{a}(x), \tag{22}$$

where $\hat{\delta}$, $\hat{\mu}$, and $\hat{a}$ are the predicted values of the model parameters under different sensor states, α_i^{δ}, α_i^{u}, and α_i^{a} are the unknown weight coefficients of different PRS model, and $\psi_i^{\delta}(x)$, $\psi_i^{u}(x)$, and $\psi_i^{a}(x)$ are the functions correlated with the physical properties of different PRS model. The PRS model is selected as the parameter training model because the model overfitting and reducing the influence of the noise data can be prevented by increasing the training data in the process of the polynomial fitting curve. By contrast, the KRG model, as an internal interpolation method, can generate a large predicted error when there are outliers in the training data [30]. The details of the role of these parameters in the proposed M-LFM method using a two-dimensional problem are taken as an example to elucidate the concept of the compensation ratio and the size of the influence domain.

Figure 2 shows the influence domain centered at the compensation point. For the three model parameters introduced, the ratio size, radius of the influence domain, and location of the compensation point were affected by a, δ, and μ, respectively. The three parameters are optimized based on the simulation and test data, which can realize the application of the M-LFM method in the SPI-DT framework. According to the parameter values predicted by the parameter model, a mathematical model that can accurately describe the structural performance in the current state is determined.

4 An engineering problem: SPI-DT of the telescopic boom crane

Here, an accurately and rapidly digital twin model of the telescopic boom crane is implemented based on our proposed framework. As a typical mechanical structure, during the telescopic process, the mutual movement of the segments of the telescopic boom crane causes the stress concentration area to dynamically change, which brings adversity to the model prediction. Therefore, the digital twin of the telescopic boom crane is seen as a research example to verify the predicted performance of the proposed framework for complex mechanical structures. Note that the programs were accomplished on a desktop personal computer with an Intel Core i7-8700 K 3.70 GHz processor and 32 GB of RAM.

4.1 Numerical simulation of the telescopic boom crane

The telescopic boom crane is an important branch of all-terrain cranes. It is composed of geometrically separated

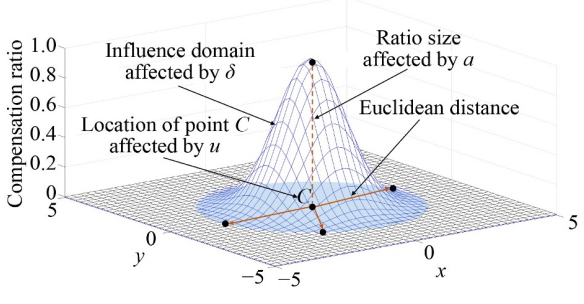

Fig. 2 Illustration of the effect of model parameters changes on the results.

telescopic boom segments to increase its working load and expand its working range [31]. During the operation of the telescopic boom crane, the main load-bearing component is the boom. The materials used for the boom have the following properties: high strength steel S690, yield limit is 690 MPa, modulus of elasticity is 210 GPa, and Poisson's ratio is 0.3 [32]. Structural failure due to fatigue damage is avoided by studying the mechanical characteristics of the boom in the working process, which is an essential way to improve the economic benefits of enterprises.

The telescopic boom crane can be divided into four segment booms: luffing hydraulic cylinder, telescopic hydraulic cylinder, leveling hydraulic cylinder, and the transmission chain between segments of the boom, as shown in Fig. 3. The mutual movement between the different segments is realized by the sliding friction of the slider, which causes the load to be transmitted from the inner segment boom to the outer segment boom. Due to the sliders being distributed at the front of the outer segment boom and the rear of the inner segment boom, the slider placed on the outer segment can be regarded as stationary, whereas the slider on the inner segment is regarded as sliding. The performance calculation of a telescopic boom often faces problems, such as strong nonlinearity and large-scale calculation, in the process of modeling and analysis due to its complex structure and large volume, resulting in an abnormally slow calculation efficiency. Therefore, the multistep quasi-static analysis method for the mechanical analysis of the telescopic boom crane solves the disadvantage of long calculation time for the dynamic analysis. The dynamic equation can be expressed as follows:

$$\boldsymbol{M}\ddot{\boldsymbol{Q}}(t)+\boldsymbol{C}\dot{\boldsymbol{Q}}(t)+\boldsymbol{K}\boldsymbol{Q}(t)=\boldsymbol{F}(t), \tag{23}$$

where t is time, $\boldsymbol{M}$, $\boldsymbol{C}$, and $\boldsymbol{K}$ represent the mass matrix, damping matrix, and stiffness matrix, respectively, $\ddot{\boldsymbol{Q}}$, $\dot{\boldsymbol{Q}}$, and $\boldsymbol{Q}$ is respectively the acceleration vector, velocity vector, and displacement vector, and $\boldsymbol{F}$ is force vector. The influence of the damping effect can be ignored in the structural analysis because the operation of the telescopic boom crane can be regarded as a low damping system by the grease lubrication.

Figure 4 shows the comparison of the displacement, velocity, and acceleration during the telescopic process. By analyzing the operating state of the telescopic boom, the velocity only fluctuates during the start and stop of the operation, which means that the telescopic process can be regarded as a uniform motion process. Therefore, the telescopic process can be considered as the transition from one equilibrium state to another continuously [33]. The mechanical equation can be expressed as follows:

$$\boldsymbol{K}\boldsymbol{Q}(t)=\boldsymbol{F}(t). \tag{24}$$

Figure 5 shows the comparison of test stress of the telescopic boom under different operating speeds. The stresses in the slow-motion state and the fast-motion state are very close, whether in the extension process or the retraction process. During the operation, there are small fluctuations in the test data, which may be due to human manipulation of the equipment. Therefore, it also proves that the influence of the operating speed of the equipment on the boom stress is very small, and the quasi-static method is effective to realize the simulation of the telescopic boom.

Another fundamental problem is that the driven system must be equivalent in the process of finite element modeling of the telescopic boom. Figure 6 shows an equivalent diagram of the driven mechanism. The telescopic cylinder as the power source drives segment 2 to move forward, and then, pulleys 1 and 2 drive segments 3 and 4 outstretch in the extension process, respectively, as shown in Fig. 6(a). Similarly, the driven system of the retraction process is the green pulley and chain. The equivalent analysis of the driven system is conducted to simplify calculation complexity and improve calculation efficiency since the driven system

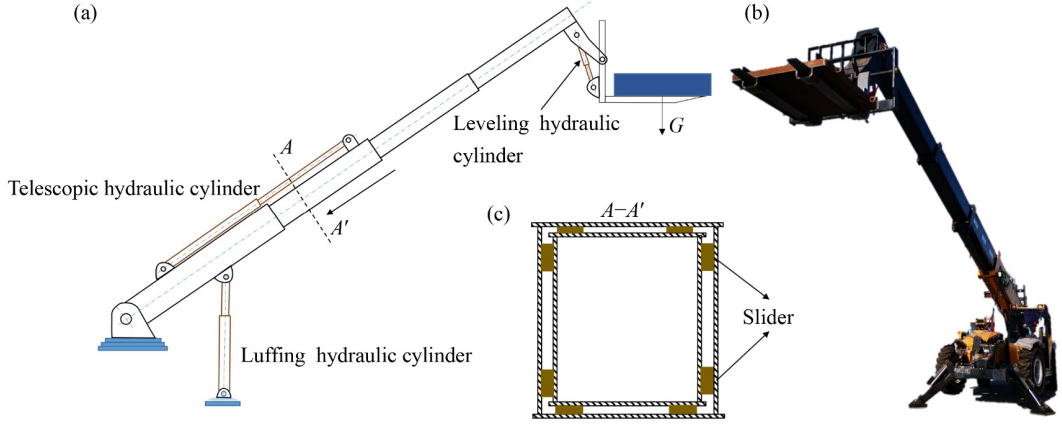

Fig. 3 Schematic diagram of the telescopic boom crane: (a) front view, (b) physical structure of the telescopic boom crane, and (c) sectional view of segment 2.

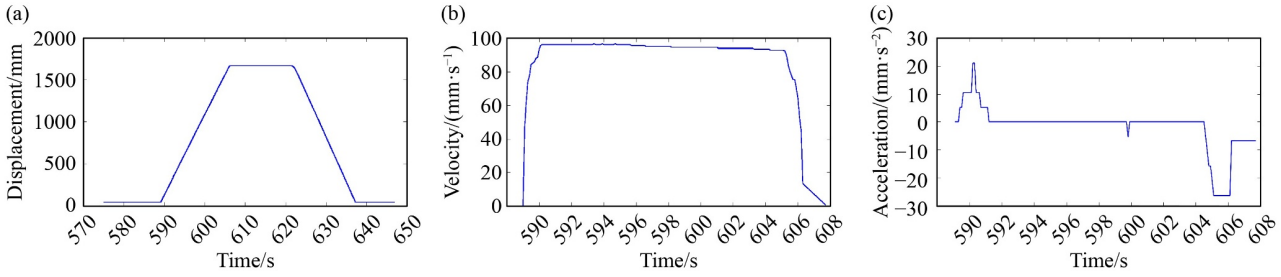

Fig. 4 Comparison of the (a) displacement, (b) velocity, and (c) acceleration in the telescopic process.

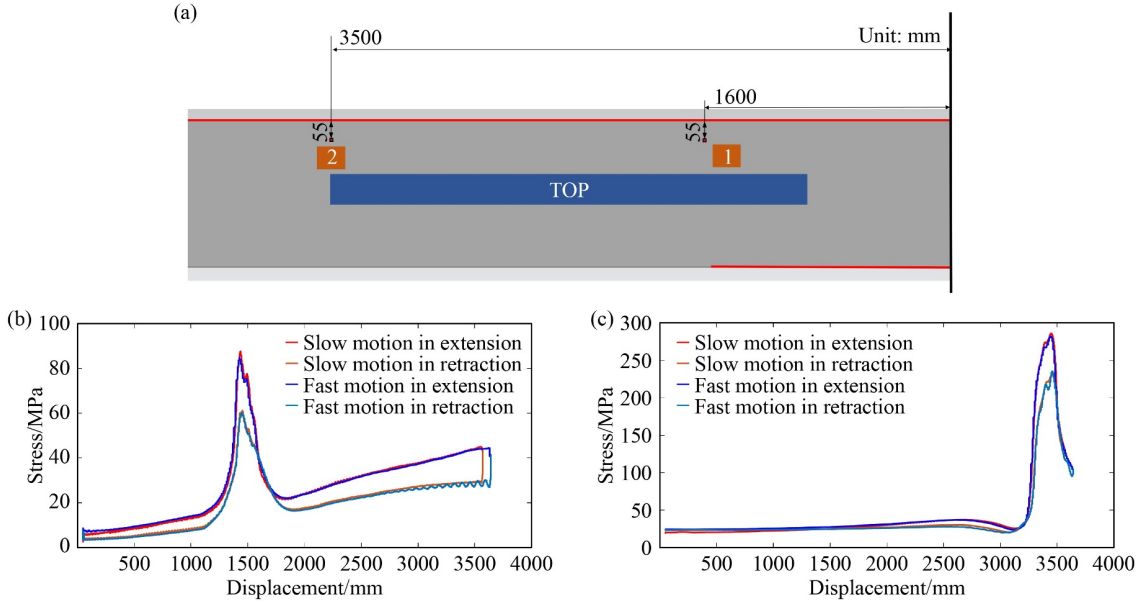

Fig. 5 Comparison of test stress of the boom under different operating speeds: (a) position distribution of gauges, test stress of the boom at (b) gauge 1 and (c) gauge 2.

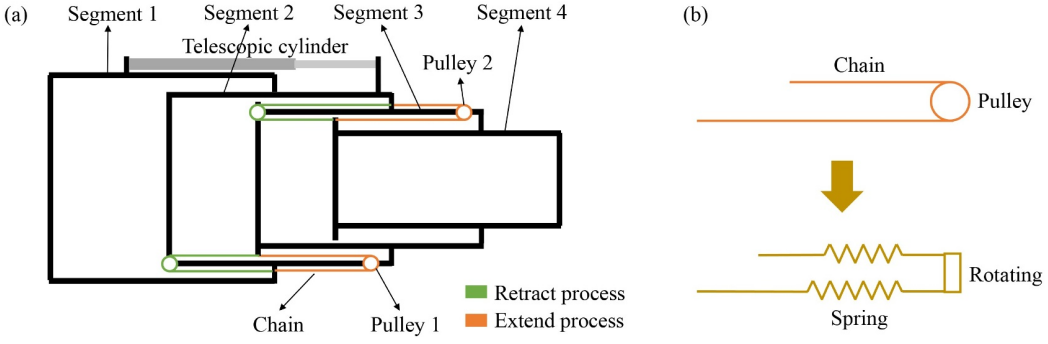

Fig. 6 Schematic diagram of the driven system: (a) driven form and (b) equivalent form.

has problems, such as high nonlinearity and load uncertainty. The pulley and chain transmission system are simplified as a combination of spring and rotating pair, as shown in Fig. 6(b). Assuming that the telescopic boom is in a horizontal static equilibrium state, then the force balance equation can be expressed as the following:

$$\begin{cases} F_5 = F_4 = F_{f4}, \\ F_3 - F_4 - F_5 + F_{f4} - F_{f3} = 0, \\ F_2 = F_3, \\ F_1 - F_2 - F_3 + F_{f3} - F_{f2} = 0, \end{cases} \tag{25}$$

where F_i $(i = 1,2,...,5)$ respectively represents the thrust produced by the hydraulic cylinder and the pulling force

produced by the transmission chain, and F_{fi} $(i=2,3,4)$ represents the fraction between segments. The difference in friction between the segments is ignored due to the grease lubrication method used in the movement of the telescopic boom. Equation (25) can be simplified as the following:

$$\begin{cases} F_4 = F_5, \\ F_2 = F_3 = F_4 + F_5, \\ F_1 = F_2 + F_3 + F_4 + F_5. \end{cases} \tag{26}$$

The finite element method (FEM) in the horizontal state is solved by applying a cylinder force of $F_1 = 120000$ N, which can be used to obtain the forces between the springs ($F_2 = 43120$ N, $F_3 = 40329$ N, $F_4 = 19824$ N, $F_5 = 19951$ N). The equivalent method can be considered reasonable according to the result that satisfies the reduced equilibrium condition.

4.2 Building an SPI-DT of the telescopic boom crane

The established process of the digital twin model for a telescopic boom crane can be divided into four steps. First, the external instantaneous parameters that affect the structural stress should be determined and transmitted by suitable sensors and communication methods. Second, the stress value and optimal parameter can be obtained by combining simulation data and measured data under different variables, which can realize the performance prediction in real-time. Third, the visualization and interaction of the telescopic boom crane on the personal computer are completed through computer graphics technology. Finally, the RUL of the boom is calculated by combining the rainflow counting method and the linear cumulative damage theory.

4.2.1 Data generation and communication

Given the complexity of the telescopic boom system and many external influencing factors, implementing all external loads of the system into the digital twin system is difficult. Therefore, the sensor data, including weight load, cylinder displacement, luffing angle, and cylinder pressure, that can reflect the state of the system are selected as the research parameters, considering the different operating modes of the telescopic boom. The sensor data are transmitted to the personal computer through the CANDTU-200UWGR communication device after reading the device's information. The CANDTU-200UWGR device can upload data on the CAN bus to the designated server since it supports 4G communication. Figure 7 shows the collection and transmission of sensor data. In the sensors used in this study, the sampling frequency of the displacement sensor, pressure sensor, and rotary encoder were all 10 ms, i.e., 100 Hz. Based on the CANDTU-200UWGR device, the data are sent to the PC in real time at a 100 ms storage interval through the 4G communication.

Besides reading sensor data in real-time, training data for the predictive model should also be generated. To obtain the stress information according to the selected variable and the test data, the FEM of the telescopic boom is calculated. The prediction model is divided into two: the extension model and the retraction model, both of which select multiple training states to complete the construction of the digital twin model.

4.2.2 Building the predicted model based on the M-LFM method

The M-LFM method is proposed to realize the black-box relationship between the stress and input variable to satisfy the high-accuracy and real-time requirements of the telescopic boom. The sensor data that can reflect the state of the telescopic boom crane are selected as the input variables, as described in Section 4.2.1. The functional relationship between the equivalent stress and the input variables can be expressed as the following:

$$\begin{cases} \boldsymbol{\sigma}_{\mathrm{s}} = \text{M-LFM}(\boldsymbol{X}), \\ \boldsymbol{\sigma}_{\mathrm{H}} = \text{M-LFM}(\boldsymbol{X}), \end{cases} \tag{27}$$

where $\boldsymbol{\sigma}_{\mathrm{s}}$ and $\boldsymbol{\sigma}_{\mathrm{H}}$ are the predicted stresses in the extension and retraction processes, respectively. The

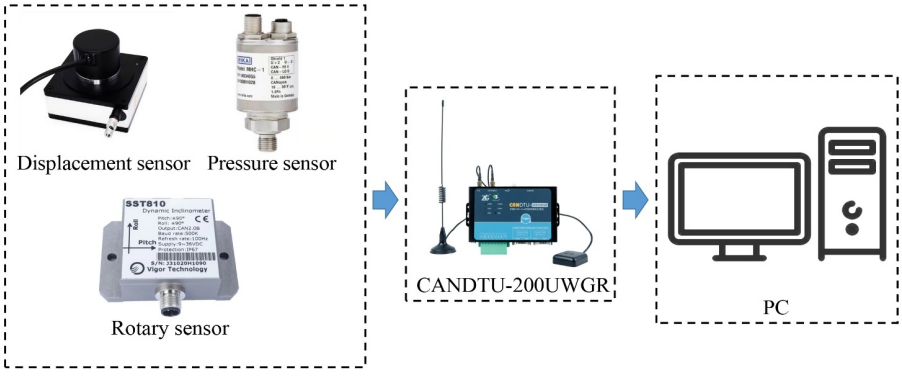

Fig. 7 Collection and transmission of sensors data.

M-LFM method was exploited to predict the performance of the telescopic boom during the extension and retraction processes. Nevertheless, determining the values of model parameters $\{\delta,\mu\}$ is a critical issue that should be solved using the optimization problem. The optimal parameters of each training state are determined by establishing a regression model and minimizing the error in the training state. To determine the values of $\{\delta,\mu\}$, 440 training states are selected for both the extension process and the retraction model:

$$\begin{aligned}&\text{for } j = 1:440\\ &\quad e_j = \min\left(\sum_{i=1}^{N}(y^i_{\text{train}\_j} - \hat{y}^i_j)^2\right)\\ &\quad \text{s.t. } \delta_{\text{l}} < \delta_j < \delta_{\text{u}},\ \mu_{\text{l}} < \mu_j < \mu_{\text{u}}\\ &\text{end}\end{aligned} \tag{28}$$

Another crucial issue in establishing the M-LFM method is determining the scale coefficient a. To do so, two methods can be used: One is based on empirical knowledge, and the other is using test data to resolve the value of the parameter. The method based on empirical knowledge often brings inestimable errors due to the uncertainty of the equipment. The compensation method based on the strain gauge is selected to determine the parameter values. To measure the stress data, 11 strain gauges were arranged on the top plate and the right plate of the boom. Among them, strain gauge Nos. 1–6 can be used to calculate the scale factor a and test the accuracy of the M-LFM method, whereas strain gauge Nos. 7–11 can be used only to evaluate the accuracy of the M-LFM method. Figure 8 shows the layout of the strain gauges. The optimal value of a under the test states can be obtained using Eq. (24) and the obtained test data. This optimal value of a can be used in the prediction model of a to achieve the accuracy improvement of the M-LFM method. To calculate the optimal value during the operation of the telescopic boom crane, 92 test points were selected, as shown in Eq. (29):

$$\begin{aligned}&\text{for } i = 1:92\\ &\quad a_i = \frac{T_i^{\text{test}} - \hat{y}_i^{\text{PRS}}}{bCf_i^{\text{nor}} \cdot \hat{y}_i^{\text{PRS}}}\\ &\text{end}\end{aligned} \tag{29}$$

The optimal values of the parameters under each training state are determined after optimization. The PRS model can be used to fit the optimal values of the parameters. Because much training data have more noise to affect the prediction performance, the PRS model is exploited to fit optimal parameters since it can filter noise. However, potential problems with the order of the PRS model will affect the predicted accuracy of the M-LFM method. The best order of the PRS model that affects the prediction accuracy of the parameter model is determined by comparing the optimal parameter training and prediction data. To complete the construction of the M-LFM method, the third-order parameter model of $\{\delta,\mu\}$ and the first-order parameter model of a were selected for prediction, as shown in Fig. 9. As the most critical component of the telescopic boom digital twin, the predictive performance of the M-LFM method will have an enormous impact on the interaction of the digital twin in the physical space and the virtual space. The stress prediction of the digital twin in a virtual space can be accurately and rapidly realized by constructing a mature M-LFM method, but structural health monitoring and

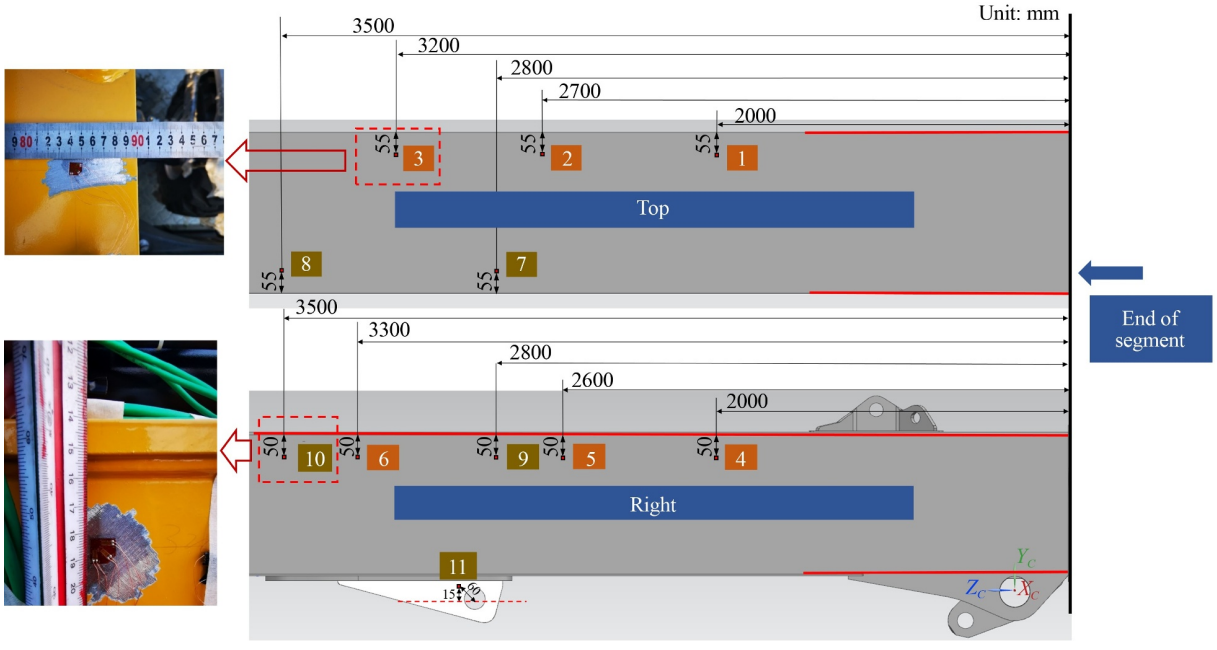

Fig. 8 Location of measured gauges in segment 1.

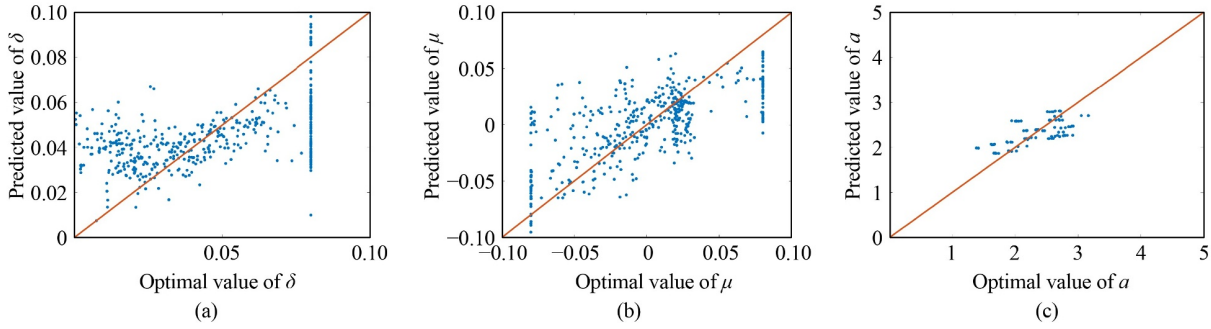

Fig. 9 Comparison of the accuracy of parameter fitting models at different orders: (a) third-order PRS model of δ, (b) third-order PRS model of μ, and (c) first-order PRS model of a.

fatigue failure prevention will have broad application prospects in the future.

4.2.3 Dynamic visualization and interaction

To build the dynamic visualization and interaction of digital twins for telescopic boom, the components involved in the SPI-DT framework are categorized as follows:

• Sensor data: the input of the digital twin. It comprises the weight load, cylinder displacement, luffing angle, and cylinder pressure.

• Geometric model: This model can build the relationship of the geometric component. It outputs the information on elements and the coordinate data of the node.

• Physical model: This model can realize the performance analysis of the geometric model. It outputs the information on performance (stress/strain) and the boundary conditions.

• Data model: The prediction model is based on the M-LFM method, which can simplify the performance analysis process and build a connection between the behavior and rules of the physical model and the virtual space.

The geometric model is obtained after the 3D model is discretized by the FEM, which can obtain the relationship between the nodal coordinate and the information of the element. The calculation time and accuracy of the FEM are related to the size of the mesh. Then, the performance results can be obtained by solving the FEM under the different boundary conditions. Based on the performance results and under the boundary conditions, the prediction model can be trained using the M-LFM method, which can build the relationship between the sensor and the performance data. Finally, the dynamic sensor data can be transmitted to the trained prediction model through the CANDTU-200UWGR, which enables the connections between the physical and digital world.

Visualization is the theory and technology of using computer graphics and image processing technology to convert data into graphics or images displayed on a screen and perform interactive processing [34]. The data visualization of predictive performance is a critical part of the construction process of the digital twin, which has certain guiding significance for the technicians. The purpose of establishing a visualized 3D telescopic boom crane model is not only to show the appearance of the model but, more importantly, to establish an information exchange and feedback mechanism to express the appearance and internal information of the model as flexibly as possible [35]. The prediction data, graphics library, and 3D dynamic simulation were integrated with the process of 3D model reconstruction. Simultaneously, the telescopic boom model is locally optimized to improve the image quality under the premise of ensuring a real-time image acquisition, which can realize the multi-detail stereo display to obtain a real 3D model. By acquiring dynamic sensor data, the dynamic visualization in the digital twin enables real-time calculation of the M-LFM method, which can dynamically render the mechanical properties of the structure to the personal computer in real time, as shown in Fig. 10. A detailed demonstration of the digital twin of the telescopic boom can be seen in the Electronic Supplementary Materials. During the operation of the telescopic crane, the dynamic display of the boom stress has an important impact on the monitoring, evaluation, and maintenance of the crane, which can prevent structural fatigue failure and reduce similar risk of an accident.

4.2.4 RUL prediction

Fatigue life refers to the number of cycles experienced in the structure before failure occurs under cyclic loading. In other words, the fatigue life refers to the duration from the beginning of the load to the final fracture. The structural component with a shorter fatigue life has a higher level of stress. To ensure the safe and stable operation of telescopic boom cranes and avoid the occurrence of fatigue accidents during the service period, fatigue life prediction is essential. Here the remaining fatigue life of the boom is calculated by Miner's linear damage rule combined with the rainflow counting

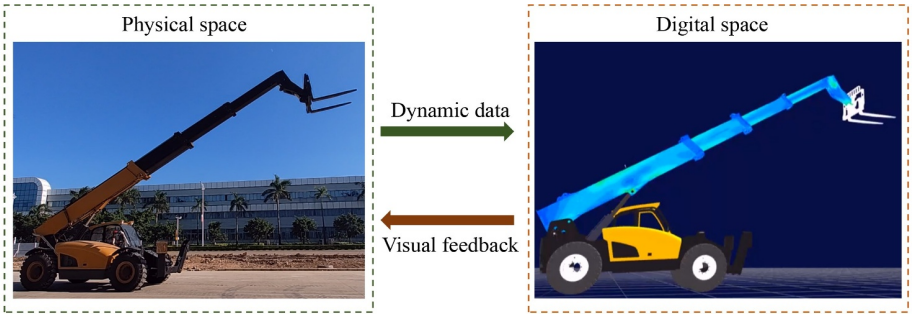

Fig. 10 Dynamic visualization of telescopic crane boom.

method, which is based on the equivalent stress of the boom during operation predicted using the M-LFM method. First, the fatigue curve of S690 steel is determined according to Ref. [36]:

$$\left(\frac{\Delta\sigma_{\text{nom}}}{2}\right)^2 = \frac{E^2}{K_{\text{t}}^2}\left\{\left[0.0067(2N_{\text{f}})^{-0.087}\right]^2 + 0.005(2N_{\text{f}})^{-0.896}\right\}, \tag{30}$$

where E is elastic modulus, N_{f} is the number of cycles to failure, $\Delta\sigma_{\text{nom}}$ is the nominal stress range, and K_{t} is the elastic stress concentration factor. In the fatigue analysis of the telescopic boom crane, the elastic stress concentration factor is $K_{\text{t}} = 2.25$ for a structural component characterized by a given nominal stress range [20]. Figure 11 shows a curve corresponding to the standard curve of S690 steels.

Using the fatigue curve to estimate the fatigue life, the actual working cyclic stress should be converted into symmetric cyclic stress. Based on the tensile yield limit, Soderberg's theory is then used to correct the mean stress:

$$\frac{\sigma_{\text{a}}}{\sigma_{\text{e(Soder)}}} + \frac{\sigma_{\text{m}}}{\sigma_{\text{y}}} = 1, \tag{31}$$

where σ_{a} is the stress amplitude, σ_{m} is the mean stress, σ_{y} is the tensile yield stress, and $\sigma_{\text{e(Soder)}}$ is the modified mean stress. The working load of many mechanical components is random in engineering practice. This load is analyzed and described using statistical analysis methods. The rainflow counting method, referred to as the rainflow method, is the most widely used method among many counting methods. The 3D data of load mean value, amplitude, and cycles can be obtained using the rainflow method [37]. The data predicted within a period will be turned into fully enclosed data that only needs to be counted once to reduce the statistical time, which means the fatigue analysis does not need to be performed in real time. The four-peak valley rainflow counting method [38] is used to extract the cycle and record the changing range of structural stress. Finally, the remaining fatigue life is calculated through Miner's linear damage rule [39] based on the statistics of the corresponding cycle times under different equivalent stress.

$$D_{\text{f}} = 1 - \sum_{g=1}^{M_g} \frac{n_g}{N_g}, \tag{32}$$

where D_{f} is the RUL, M_g is the total cycle number, and n_g and N_g are the cycle numbers in practical and cycles to failure under the gth cycles, respectively.

4.3 Results and discussion

4.3.1 Prediction results of the M-LFM method

According to the finite element analysis and the knowledge of structural mechanics, the contact area of the slider at the boom will cause the stress concentration and the phenomenon dynamic changes with the movement position of the slider. When the telescopic cylinder is extended forward, the point of maximum stress will move forward, as shown in Fig. 12. The upper plate is warped due to the contact of the upper slider, which causes the side plate to dent inward, thereby maximizing the stress at the welding seam.

To verify the accuracy and applicability of the model in the establishment of an SPI-DT, strain gauges were

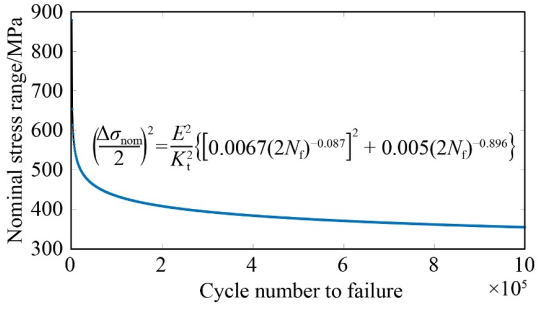

Fig. 11 Fatigue curve of S690 steels applied in telescopic boom crane.

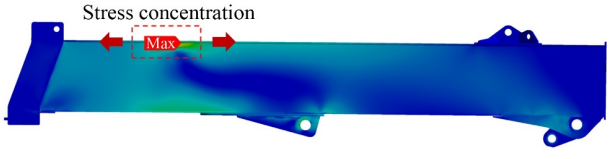

Fig. 12 Stress distribution of finite element model in segment 1.

placed on segment 1 of the boom to test the stress and compared with the predicted results of the model. The measured stress, the PRS model predictive stress, the KRG model predictive stress, and the M-LFM method predictive stress were compared by reading the sensor data and changing the operating conditions. Given numerous selected measuring points, the test process is divided into two: The measured stress at gauge Nos. 1–6 was obtained to ensure the scale factor a for the first time, and the measured stress at gauge Nos. 7–11 was obtained to ensure the scale factor a for the second time. Figures 13(a)–13(c) show the comparison of stress at compensation gauge Nos. 1, 3, and 5. Figures 13(d)–13(f) show the comparison of stress at test gauge Nos. 7, 9, and 11. The prediction results of the M-LFM method are consistent with the test results in multiple cycles. According to the test data in Fig. 13(b), the slider has a peak when it passes the test point, but a peak cannot appear when it does not pass the test point. The reason for this phenomenon is that the contact area of the slider is the main force position of the telescopic boom, where the warping of the top of the boom causes dynamic stress concentration on the side and top plates. However, the peak stress does not exist when the gauges are far away from the contact area of the slider. Figure 13(f) compared with the other five images is inconsistent with the stress trend since the strain gauge is located near the hinge hole and is not affected by the contact area of the slider.

Although it can be seen in Fig. 11 that the predicted stress of the M-LFM method and test stress can maintain good consistency under multiple cycles, the comparison of local details is unclear. To more intuitively observe the advantages of the M-LFM method compared with other models, the prediction results of the M-LFM method and the equivalent stress of the measured gauge are compared in a single period, as shown in Fig. 14. The blue, brown, black, and purple curves represent the test result of the strain gauge, the prediction result of the M-LFM method, the prediction result of the PRS model, and the prediction result of the KRG model, respectively. The results predicted using the M-LFM method are consistent with the test results of the strain gauges at the measuring point, whereas the PRS model does not reflect the trend of stress changes in the contact area of the slider, as shown in Fig. 14. Although the KRG method can predict the changing trend of stress, there is a large error in the predicted value. The prediction results of the M-LFM method agree well with the PRS method since this area is not affected by the dynamic stress concentration in this case, as shown in Fig. 14(f). The prediction results are poor because the KRG model is an interpolation model affected by the training data. In short, the M-LFM

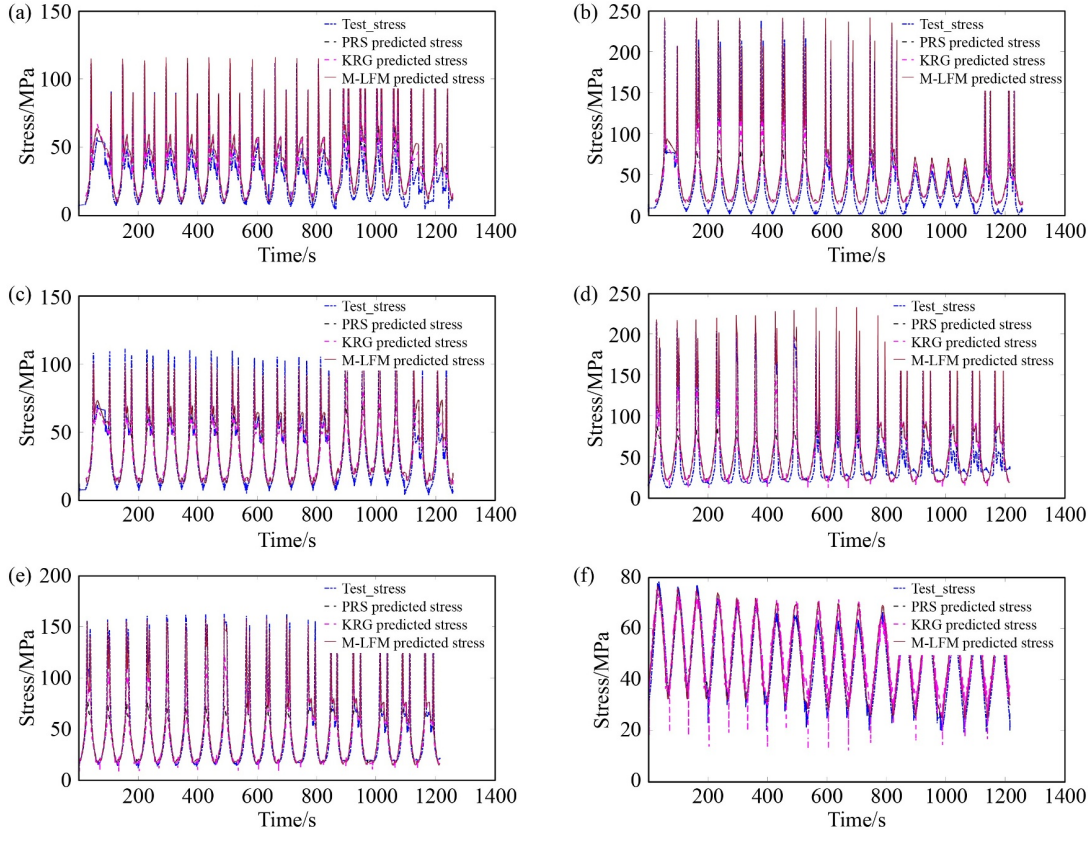

Fig. 13 Comparison of global equivalent stress at measured gauge: (a) gauge 1, (b) gauge 3, (c) gauge 5, (d) gauge 7, (e) gauge 9, and (f) gauge 11.

method compared with the PRS and KRG models can better reflect the stress changes at the strain gauge.

To quantify the prediction performance of the M-LFM method, the coefficient of determination R^2, the normalized root mean square error (NRMSE), and the normalized maximum absolute error (NMAE) [40,41] are selected as the evaluation criteria for the accuracy of the model. The coefficient of determination is the most intuitive evaluation standard reflecting the fitting performance of the model, which can be calculated based on the error between the predicted value of the model and the true response at the test point. The expression is as follows:

$$R^2 = 1 - \frac{\sum_{i=1}^{N_t} (y_i - \hat{y}_i)^2}{\sum_{i=1}^{N_t} (y_i - \bar{y})^2}, \tag{33}$$

where y_i is the true output of the problems at the test point x_i, $\hat{y}_i$ is the predicted response of the M-LFM method at the test point x_i, $\bar{y}$ is the mean value of the true output at all test points, and N_t is the number of test points. R^2 varies from 0 to 1, so the prediction model is closer to the real model when the value of R^2 is closer to 1. NRMSE is also a method commonly used to evaluate the error between the predicted value and the true value on the overall design space. The expression of the NRMSE is as follows:

$$\mathrm{NRMSE} = \frac{1}{\max(\boldsymbol{y}) - \min(\boldsymbol{y})} \cdot \sqrt{\frac{1}{N_t} \sum_{i=1}^{N_t} (y_i - \hat{y}_i)^2}. \tag{34}$$

The NRMSE should be as small as possible for a model with high prediction accuracy. The range of the NRMSE is greater than 0, and its amplitude is affected by the output amplitude of the original problem. The above two metrics, R^2 and NRMSE, evaluate the model prediction accuracy from the perspective of the overall design space, but the NMAE is an evaluation standard for the local error of the model. The NMAE is used to calculate the maximum error between the predicted value and the response value at the test point. The expression of the NMAE is as follows:

$$\mathrm{NMAE} = \max|\boldsymbol{y} - \hat{\boldsymbol{y}}| \Big/ \sqrt{\frac{1}{N_t} \sum_{i=1}^{N_t} (y_i - \hat{y}_i)^2}. \tag{35}$$

The smaller the NMAE value, the higher the local prediction accuracy of the model. The accuracy of the M-LFM method, the PRS model, and the KRG model at each measuring point are calculated by taking the test results as a benchmark, as shown in Tables 1 and 2. The predicted accuracy of the M-LFM method is better than that of the PRS model and KRG model whether it is local or global accuracy, except for measuring point 11. For measuring point 11, the M-LFM method performs stress compensation based on the measured data, which shows an obvious advantage in the dynamic stress concentration area. The prediction accuracy of the KRG model is higher than that of the PRS model. This phenomenon is because the KRG model is more consistent with the measuring results trend, as shown in Fig. 14. Moreover, the results of the M-LFM method agree well with those of the PRS model in gauge No. 11 since the measurement gauge is not located in the contact area of the slider. In other

Table 1 Error evaluation of the M-LFM method and other models at the measured compensation gauge

Gauge	R^2			NRMSE			NMAE		
	M-LFM	PRS	KRG	M-LFM	PRS	KRG	M-LFM	PRS	KRG
Gauge 1	0.7695	0.3328	0.6565	0.0817	0.1389	0.0997	0.4004	3.8986	2.8094
Gauge 2	0.8073	0.4601	0.6619	0.0873	0.1462	0.1157	0.2318	3.4447	3.0076
Gauge 3	0.8767	0.4308	0.7216	0.0688	0.1478	0.1033	0.4635	4.1060	3.0413
Gauge 4	0.8984	0.5106	0.7285	0.0619	0.1359	0.1013	1.1971	3.0113	1.8970
Gauge 5	0.9124	0.6448	0.8039	0.0608	0.1225	0.0910	0.4667	3.5099	3.1189
Gauge 6	0.9592	0.6151	0.7771	0.0422	0.1298	0.0987	0.1153	3.1424	3.3241

Table 2 Error evaluation of the M-LFM method and other models at the measured test gauge

Gauge	R^2			NRMSE			NMAE		
	M-LFM	PRS	KRG	M-LFM	PRS	KRG	M-LFM	PRS	KRG
Gauge 7	0.7987	0.3875	0.6851	0.0899	0.1569	0.1125	1.0463	3.8506	2.9158
Gauge 8	0.8395	0.4634	0.7247	0.0499	0.0913	0.0654	2.7092	7.1509	6.7679
Gauge 9	0.9289	0.5081	0.7855	0.0678	0.1782	0.1177	0.3957	3.1007	2.2368
Gauge 10	0.9436	0.5746	0.7903	0.0444	0.1013	0.0855	1.9419	5.0236	3.8413
Gauge 11	0.8797	0.8797	0.8207	0.0759	0.0759	0.0927	0.329	0.3291	0.5223

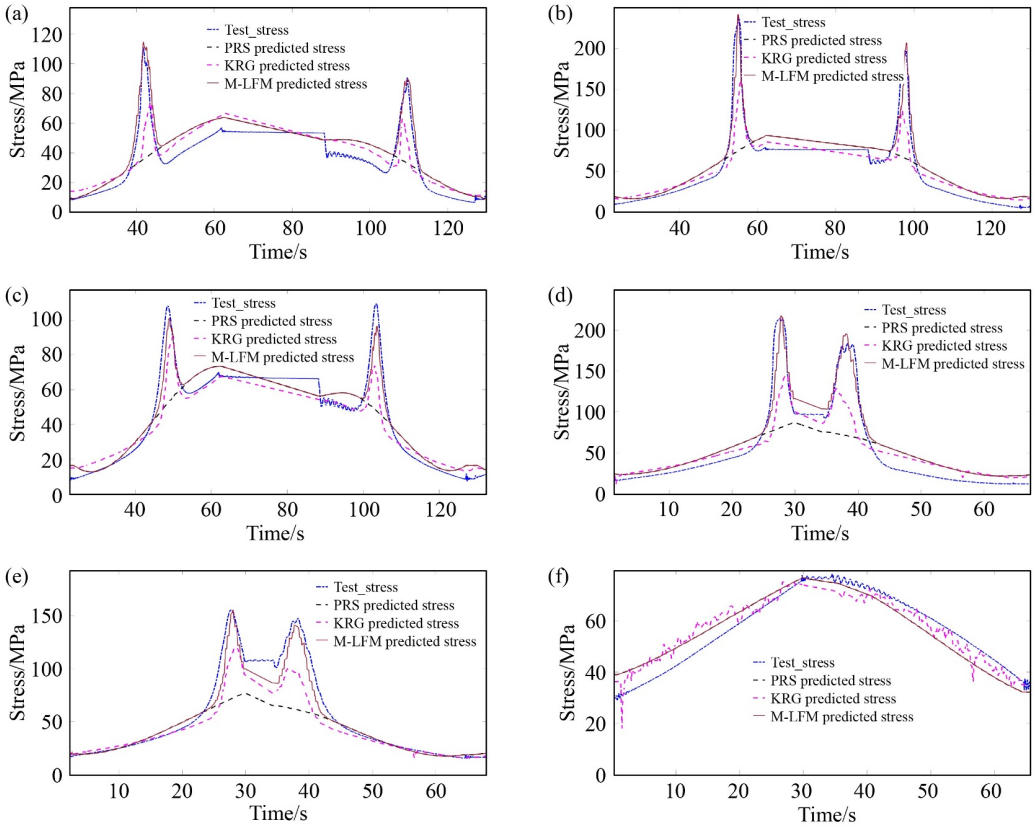

Fig. 14 Comparison of local equivalent stress of measured gauge: (a) gauge 1, (b) gauge 3, (c) gauge 5, (d) gauge 7, (e) gauge 9, and (f) gauge 11.

words, the measurement gauge located in the stress compensation area has undergone stress revision, which improves the prediction accuracy. Therefore, the M-LFM method can accurately predict the stress concentration phenomenon caused by contact changes in the mechanical structure of each component moving with each other, which can significantly improve the accuracy of the digital twin model.

Another indispensable issue to tackle for realizing the digital twin model is to ensure the real-time performance of model predictions. In the digital twin of the telescopic boom, a great challenge concerning the real-time requirements was brought forward because of the need to perform prediction calculations of multiple outputs simultaneously. To verify the real-time performance of the model prediction, the delay time of the M-LFM method, PRS model, and KRG model are compared, as shown in Table 3. The results show that the proposed M-LFM method can obtain the prediction results faster than the KRG method. However, the M-LFM method has a delay time in the prediction similar to the PRS model, which is caused by the calculation of the stress compensation.

Table 3 Comparison of delay time under different models

Model type	Delay time of the extension model/s	Delay time of the retraction model/s
M-LFM	0.447	0.458
KRG	2.302	2.106
PRS	0.446	0.456

4.3.2 Analysis of model parameters uncertainty

Due to the difference in the analyzed structure and training data, the prediction parameters fluctuate, which affects the prediction results of the model. To study the influence of the uncertainty of the model parameters on the prediction results, the signal-to-noise ratio (SNR) of Gaussian white noise was added to the predicted values of the parameters [42,43]. The expression is as follows:

$$\mathrm{SNR} = 10\lg\frac{P}{P_{\mathrm{noise}}} = 20\lg\frac{A}{A_{\mathrm{noise}}}, \tag{36}$$

where P is the power of the signal, P_{noise} is the power of the noise, A is the amplitude of the signal, and A_{noise} is the noise corresponding value. The predicted parameters with different SNR values are dynamically integrated, respectively, to more realistically simulate the online prediction of stress under real conditions. Figure 15 shows the results of these methods and analysis.

Figure 15 shows the uncertainty estimate of the M-LFM method under parameter noise, where the red shade represents the uncertainty boundary of the model in the 95% confidence interval. The uncertainty at the contact

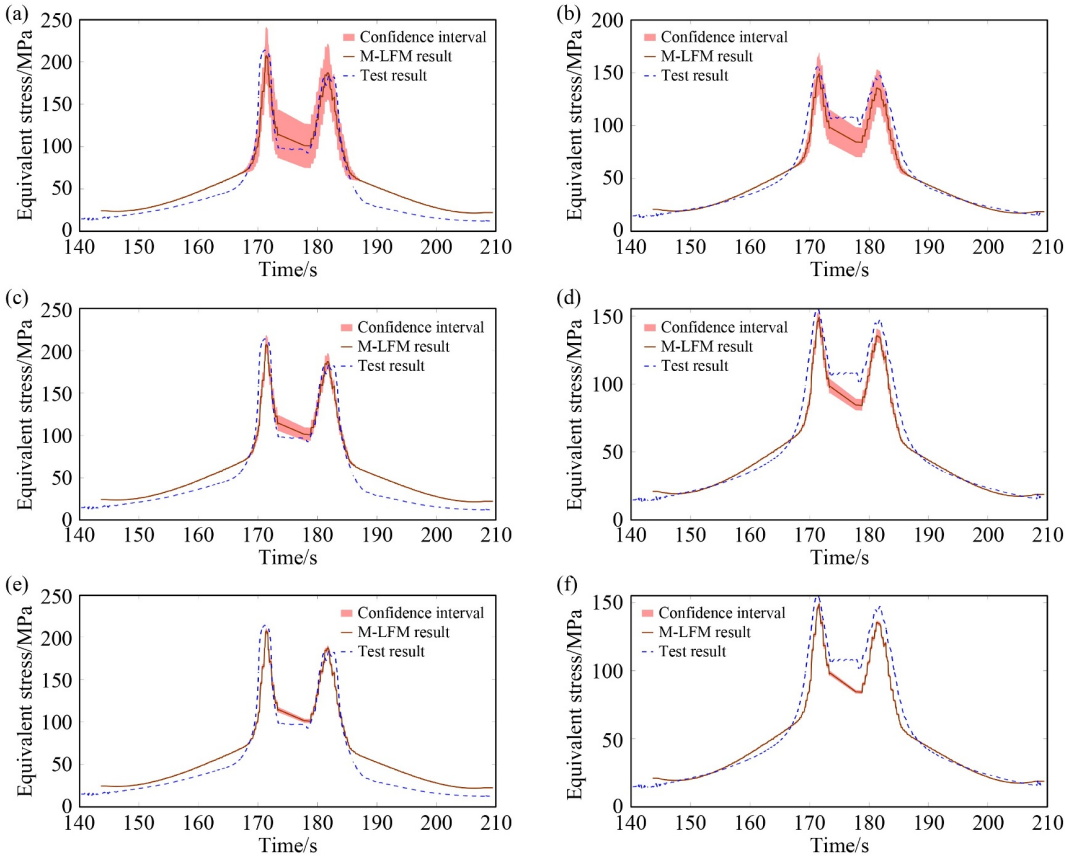

Fig. 15 Uncertainty estimate with a 95% confidence interval of the M-LFM method under parameter noise: equivalent stress of (a) gauge 7 (SNR = 10), (b) gauge 9 (SNR = 10), (c) gauge 7 (SNR = 20), (d) gauge 9 (SNR = 20), (e) gauge 7 (SNR = 30), and (f) gauge 9 (SNR = 30).

area of the slider is affected since the prediction results change with the model parameters, and the uncertainty is the largest when the state changes from the extension process to the retraction process, which is caused by the conversion from the extension model to the retraction model. Meanwhile, as shown in Fig. 15, the uncertainty can distinguish the difference in the prediction results of the M-LFM method between different SNR values. The global view represents the whole prediction results with different SNR values and the test result. It can be found that there are obvious differences between the test result and the confidence interval when the SNR was 10. However, the confidence interval of the M-LFM method does not distinguish the predicted results when the SNR is 30. Furthermore, the M-LFM method has better robustness by comparing the prediction results under different SNR values.

4.3.3 Prediction result of RUL

The experimental data obtained from the fatigue test of the telescopic boom were compared with the predicted data to verify the feasibility of the proposed digital twin model for fatigue life prediction. The fatigue test data of the telescopic boom were obtained through repeated tests on the extreme working conditions of the telescopic boom under a mass load of 26671 N (mass: ~2721.55 kg). To illustrate the applicability of the fatigue prediction model in practical engineering, the number and distribution of fatigue cycles of the telescopic boom under corresponding working conditions were predicted based on the proposed digital twin fatigue model. The measured life is 35055 times and the predicted life is 53265 times under a mass load of 26671 N. The predicted life is within two times the measured life, which demonstrates that the predicted effect of the fatigue model is good.

According to the fatigue test experience of the telescopic boom crane under actual working conditions, the fatigue failure position of the boom often occurs at the welding seam far from the end of segment 1. Figure 16 shows the comparison of measured life and predicted life calculated by the proposed digital twin framework. Figure 16(a) shows the areas of fatigue failure in the test. Figure 16(b) shows the remaining fatigue life color map of segment 1 after multiple load cycles. The weld seam away from the end of segment 1 is the most prone to failure of the boom. The obtained fatigue trend is very consistent with the actual fatigue test, which shows that

the proposed digital twin fatigue model has a certain guiding significance for operating the telescopic boom crane.

To understand the change trend of the fatigue behavior of the telescopic boom crane by the digital twin model, the remaining fatigue life at the measuring point was observed. Figure 17 shows the statistical histogram of the rainflow counting method at measuring point 7. Figure 17(a) shows the load reversals at measuring point 7 under multiple cycles. The range of the stress amplitude is 25–230 MPa at measuring point 7. Figure 17(b) shows the statistical histogram obtained using the rainflow counting method. A large number of statistics appear when the stress range is 0–20 MPa. The reason for this phenomenon is the stress fluctuation caused by the vibration of the telescopic boom crane during operation, which generates less fatigue damage to the structure. Nevertheless, a stress cycle with a large variation range will still produce large fatigue damage, even if the number of statistics is few. Figure 17(c) shows the trend of the remaining life at gauge Nos. 7–11. The farther away from the end of segment 1, the lower the fatigue life of the position, and the remaining life of the upper plate is lower than the fatigue life of the side plate.

5 Conclusions

This paper proposed an M-LFM method to construct an SPI-DT for operating equipment in real time. This method is realized by combining the advantages of the PRS and KRG models in prediction and using the Gaussian function to compensate for the surrounding area. In the implementation of the M-LFM method, three crucial model parameters were determined through the fusion of the training and test data. This significantly improves the predicted performance of the digital twin for complex engineering problems, making the digital twin model more lightweight and credible. Then, to verify the accuracy and efficiency of the M-LFM method, the digital twin of the telescopic boom crane was realized. The results showed that the proposed M-LFM method has better calculation accuracy and efficiency than the PRS and KRG models since it combines the different surrogate

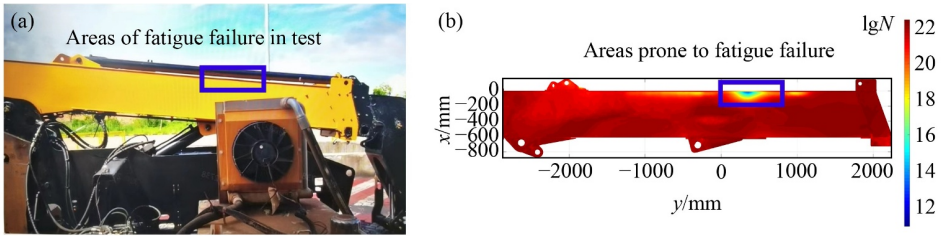

Fig. 16 Trend of remaining useful life under equivalent stress cycles: (a) trend of measured life in the fatigue test and (b) predicted life of the digital twin after multiple stress cycles.

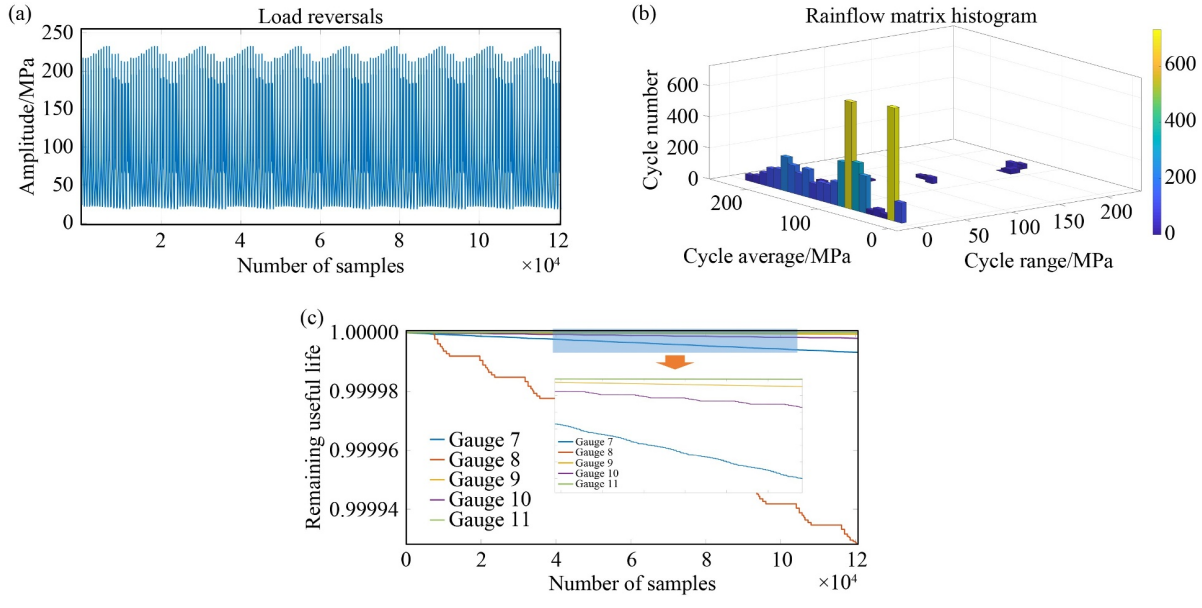

Fig. 17 Statistics of rainflow counting method at measuring point 7: (a) load history, (b) statistical histogram of the rainflow counting method, and (c) trend of remaining useful life at gauge Nos. 7–11.

models and multiple types of data. Finally, the RUL of the telescopic boom is predicted based on the rainflow counting method and Miner's linear cumulative damage theory. Noteworthy, the proposed M-LFM method, as a feasible paradigm, not only can be extended to other types of cranes and construction machinery but can also be used in aerospace, fluid machinery, and other fields.

However, the M-LFM method has limitations and inadequacies in some application scenarios. For example, if the stress concentration area of the structure cannot be determined or sensors cannot be arranged in this area, the model parameters must be determined empirically. Therefore, a direction for future research is to establish an M-LFM method for each area by reasonably dividing the stress area, which can make the algorithm more applicable. Another direction is to obtain optimal sensor layout by selecting crucial positions that have a significant impact on the analysis results from most measurement positions. As such, to efficiently maximize and improve the reliability of the monitoring information, the density of sensor information can be utilized.

Nomenclature

Abbreviations

3D	Three-dimensional
DT	Digital twin
FEM	Finite element method
KRG	Kriging
M-LFM	Multi-level fusion modeling
NMAE	Normalized maximum absolute error
NRMSE	Normalized root mean square error
PRS	Polynomial response surface
RUL	Remaining useful life
SNR	Signal-to-noise ratios
SPI-DT	Shape–performance integrated digital twin

Variables

a	Unknown coefficient used to change the result size of the predicted model
A	Amplitude of the signal
A_{noise}	Amplitude of the noise
b	Scale factor
D_{f}	Remaining useful life
e	Error between the training value and the predicted value at training point
E	Elastic modulus,
$f_i(\cdot)$ $(i = 1,2,\ldots,m)$	Unknown approximate function
F_i $(i = 1,2,\ldots,5)$	Thrust produced by the hydraulic cylinder and the pulling force produced by the transmission chain
F_{fi} $(i = 2,3,4)$	Fraction between segments
$\boldsymbol{F}$	Force vector
g	gth cycle
$\boldsymbol{H}$	Vector whose elements are ones
k	Number of measured data
K_{t}	Elastic stress concentration factor
L	Cost function
m	Number of input variables
M_g	Total cycle number
$\boldsymbol{M}$, $\boldsymbol{C}$, $\boldsymbol{K}$	Mass matrix, damping matrix, and stiffness matrix, respectively
n_g, N_g	Cycle number in practical and cycles to failure, respectively
N_{f}	Cycle number to failure
N_{t}	Test point number
P	Signal power
P_{noise}	Noise power
$\boldsymbol{Q}$, $\dot{\boldsymbol{Q}}$, $\ddot{\boldsymbol{Q}}$	Displacement, velocity, and acceleration vector, respectively
$\boldsymbol{r}$	Related vector between the unknown predicted point and the trained point
R	Relationship function
R^2	Coefficient of determination
$\boldsymbol{R}$	Relationship matrix whose elements are the value of relationship function
t	Time
$\boldsymbol{T}^{\text{test}}$	Measured data
u_i, v_i, w_i	Space coordinates in the ith point
u_C, v_C, w_C	Space coordinates in the compensation point
x_i $(i = 1,2,\ldots,m)$	ith input variable
$\boldsymbol{X}$	Input vector
$\bar{y}$	Mean value of the true output at all test points
$\hat{y}$	Predicted value of output variable
y_i^{train}	Response value in the ith training point
$\hat{\boldsymbol{y}}^{\text{PRS}}$	Predicted data of PRS model
$\hat{y}_C^{\text{PRS}}$, $\hat{y}_C^{\text{KRG}}$	Predicted values of the PRS model and KRG model at the compensation point, respectively
$\boldsymbol{y}_{\text{s}}$	True response value at samples.
$\boldsymbol{Y}$	Output vector
$\boldsymbol{Y}_{\text{PRS}}$, $\boldsymbol{Y}_{\text{KRG}}$	Predicted vectors of the PRS model and the KRG model, respectively
$z(\cdot)$	Error function of KRG model
Cf_i $(i = 1,2,\ldots,n)$	Compensation factor of the influence domain
$Cf_{\min}$, $Cf_{\max}$	Minimum and maximum values of the compensation factor set, respectively

Cf_i^{nor}	Normalized compensation factor
$\boldsymbol{Cf}_{\mathrm{nor}}$	Compensation factor set
α_i $(i=1,2,\ldots,m)$	Unknown weight coefficient
α_i^{δ}, α_i^{μ}, α_i^{a}	Unknown weight coefficient of different parameters model
$\boldsymbol{\alpha}$	Vector of unknown coefficients
$\hat{\beta}$	Maximum likelihood estimation value of hyper-parameter
β_i	Unknown weighted coefficients of the KRG model
δ	Parameter of the influence domain
$\hat{\delta}$, $\hat{\mu}$, $\hat{a}$	Predicted values of the model parameters under different sensor states
δ_{l}, δ_{u}	Upper and lower bounds of the parameter δ, respectively
$\boldsymbol{\delta}_{\mathrm{opt}}$, $\boldsymbol{\mu}_{\mathrm{opt}}$, $\boldsymbol{a}_{\mathrm{opt}}$	Optimal parameters of δ, μ, and a, respectively
$\boldsymbol{\varepsilon}$	Vector of error function
μ	Deviation coefficient of the compensation point
μ_{l}, μ_{u}	Upper and lower bounds of the parameter μ, respectively
ρ_i $(i=1,2,\ldots,n)$	Euclidean distance between the compensation point and the surrounding points
$\rho_{\min}$, $\rho_{\max}$	Minimum and maximum values of the Euclidean distance set, respectively
ρ_i^{nor}	Normalized Euclidean distance
σ^2	Variance of error function
σ_{a}	Stress amplitude
σ_{m}	Mean stress
σ_{y}	Tensile yield stress
$\sigma_{\mathrm{e(Soder)}}$	Modified mean stress
$\boldsymbol{\sigma}$	Performance vector
$\boldsymbol{\sigma}_{\mathrm{s}}$, $\boldsymbol{\sigma}_{\mathrm{h}}$	Predicted stresses in the extension and retraction processes, respectively
$\Delta\sigma_{\mathrm{nom}}$	Nominal stress range
$\psi_i(x)$	Function correlated with the physical properties of problem itself
$\psi_i^{\delta}(x)$, $\psi_i^{u}(x)$, $\psi_i^{a}(x)$	Functions correlated with the physical properties of different PRS model

Acknowledgements This work was supported by the National Key R&D Program of China (Grant No. 2018YFB1700704) and the National Natural Science Foundation of China (Grant No. 52075068).

Electronic Supplementary Materials The supplementary materials can be found in the online version of this article at https://doi.org/10.1007/s11465-022-0708-0 and are accessible to authorized users.

References

1. Bloem J, van Doorn M, Duivestein S, Excoffier D, Maas E, van Ommeren E. The fourth industrial revolution. Sogeti VINT2014, 2014, 8: 11–15
2. Xu M, David J M, Kim S H. The Fourth Industrial Revolution: opportunities and challenges. International Journal of Financial Research, 2018, 9(2): 90–95
3. Cekus D, Kwiatoń P, Geisler T. The dynamic analysis of load motion during the interaction of wind pressure. Meccanica, 2021, 56(4): 785–796
4. Trąbka A. Dynamics of telescopic cranes with flexible structural components. International Journal of Mechanical Sciences, 2014, 88: 162–174
5. Guivarch D, Mermoz E, Marino Y, Sartor M. Creation of helicopter dynamic systems digital twin using multibody simulations. CIRP Annals, 2019, 68(1): 133–136
6. Grieves M. Digital Twin: Manufacturing Excellence Through Virtual Factory Replication. White Paper, 2014
7. Tuegel E J, Ingraffea A R, Eason T G, Spottswood S M. Reengineering aircraft structural life prediction using a digital twin. International Journal of Aerospace Engineering, 2011, 2011: 154798
8. Tao F, Cheng J F, Qi Q L, Zhang M, Zhang H, Sui F Y. Digital twin-driven product design, manufacturing and service with Big Data. The International Journal of Advanced Manufacturing Technology, 2018, 94(9): 3563–3576
9. Jiang H F, Qin S F, Fu J L, Zhang J, Ding G F. How to model and implement connections between physical and virtual models for digital twin application. Journal of Manufacturing Systems, 2021, 58: 36–51
10. Ye Y M, Yang Q, Yang F, Huo Y Y, Meng S H. Digital twin for the structural health management of reusable spacecraft: a case study. Engineering Fracture Mechanics, 2020, 234: 107076
11. He X W, Qiu Y M, Lai X N, Li Z H, Shu L M, Sun W, Song X G. Towards a shape−performance integrated digital twin for lumbar spine analysis. Digital Twin, 2021, 1(8): 8
12. Ritto T G, Rochinha F A. Digital twin, physics-based model, and machine learning applied to damage detection in structures. Mechanical Systems and Signal Processing, 2021, 155: 107614
13. Lai X N, Wang S, Guo Z G, Zhang C, Sun W, Song X G. Designing a shape–performance integrated digital twin based on multiple models and dynamic data: a boom crane example. Journal of Mechanical Design, 2021, 143(7): 071703
14. Kapteyn M G, Knezevic D J, Huynh D B P, Tran M, Willcox K E. Data-driven physics-based digital twins via a library of component-based reduced-order models. International Journal for Numerical Methods in Engineering, 2022, 123(13): 2986–3003
15. Luo W C, Hu T L, Ye Y X, Zhang C R, Wei Y L. A hybrid predictive maintenance approach for CNC machine tool driven by digital twin. Robotics and Computer-Integrated Manufacturing, 2020, 65: 101974
16. Wang S, Lai X N, He X W, Qiu Y M, Song X G. Building a trustworthy product-level shape−performance integrated digital twin with multifidelity surrogate model. Journal of Mechanical Design, 2022, 144(3): 031703
17. Kontaxoglou A, Tsutsumi S, Khan S, Nakasuka S. Towards a digital twin enabled multifidelity framework for small satellites. In: Proceedings of the 6th European Conference of the Prognostics and Health Management Society. 2021, 211–220

18. Chetan M, Yao S L, Griffith D T. Multi-fidelity digital twin structural model for a sub-scale downwind wind turbine rotor blade. Wind Energy, 2021, 24(12): 1368–1387
19. Al Zamzami I, Susmel L. On the accuracy of nominal, structural, and local stress based approaches in designing aluminium welded joints against fatigue. International Journal of Fatigue, 2017, 101: 137–158
20. Nziu P K, Masu L M. Formulae for predicting stress concentration factors in flat plates and cylindrical pressure vessels with holes: a review. International Journal of Mechanical and Production Engineering Research and Development, 2019, 9(5): 753–770
21. Song X G, Lv L Y, Li J L, Sun W, Zhang J. An advanced and robust ensemble surrogate model: extended adaptive hybrid functions. Journal of Mechanical Design, 2018, 140(4): 041402
22. Lai X N, He X W, Wang S, Wang X B, Sun W, Song X G. Building a lightweight digital twin of a crane boom for structural safety monitoring based on a multi-fidelity surrogate model. Journal of Mechanical Design, 2022, 144(6): 064502
23. Sun G Y, Song X G, Baek S, Li Q. Robust optimization of foam-filled thin-walled structure based on sequential kriging metamodel. Structural and Multidisciplinary Optimization, 2014, 49(6): 897–913
24. Chakraborty S, Adhikari S, Ganguli R. The role of surrogate models in the development of digital twins of dynamic systems. Applied Mathematical Modelling, 2021, 90: 662–681
25. Khuri A I, Mukhopadhyay S. Response surface methodology. Wiley Interdisciplinary Reviews: Computational Statistics, 2010, 2(2): 128–149
26. Cressie N. The origins of kriging. Mathematical Geology, 1990, 22(3): 239–252
27. Fuhg J N, Fau A, Nackenhorst U. State-of-the-art and comparative review of adaptive sampling methods for kriging. Archives of Computational Methods in Engineering, 2021, 28(4): 2689–2747
28. Grieves M, Vickers J. Digital twin: mitigating unpredictable, undesirable emergent behavior in complex systems. In: Kahlen J, Flumerfelt S, Alves A, eds. Transdisciplinary Perspectives on Complex Systems. Cham: Springer, 2017, 85–113
29. Tao F, Zhang H, Liu A, Nee A Y C. Digital twin in industry: state-of-the-art. IEEE Transactions on Industrial Informatics, 2019, 15(4): 2405–2415
30. Bhosekar A, Ierapetritou M. Advances in surrogate based modeling, feasibility analysis, and optimization: a review. Computers & Chemical Engineering, 2018, 108: 250–267
31. Savković M, Gašić M, Pavlović G, Bulatović R, Zdravković N. Stress analysis in contact zone between the segments of telescopic booms of hydraulic truck cranes. Thin-Walled Structures, 2014, 85: 332–340
32. Yao J, Xing F, Fu Y Q, Qiu X M, Zhou Z P, Hou J H. Failure analysis of torsional buckling of all-terrain crane telescopic boom section. Engineering Failure Analysis, 2017, 73: 72–84
33. Liao J B, Tang G W, Meng L B, Liu H G, Zhang Y J. Finite element model updating based on field quasi-static generalized influence line and its bridge engineering application. Procedia Engineering, 2012, 31: 348–353
34. Liu P, Gong J H, Yu M. Visualizing and analyzing dynamic meteorological data with virtual globes: a case study of tropical cyclones. Environmental Modelling & Software, 2015, 64: 80–93
35. Wang Q Y, Jiao W H, Zhang Y M. Deep learning-empowered digital twin for visualized weld joint growth monitoring and penetration control. Journal of Manufacturing Systems, 2020, 57: 429–439
36. de Jesus A M P, Matos R, Fontoura B F C, Rebelo C, Simões da Silva L, Veljkovic M. A comparison of the fatigue behavior between S355 and S690 steel grades. Journal of Constructional Steel Research, 2012, 79: 140–150
37. Dong Q, He B, Qi Q S, Xu G N. Real-time prediction method of fatigue life of bridge crane structure based on digital twin. Fatigue & Fracture of Engineering Materials & Structures, 2021, 44(9): 2280–2306
38. Liu X T, Zhang M H, Wang H J, Luo J, Tong J C, Wang X L. Fatigue life analysis of automotive key parts based on improved peak-over-threshold method. Fatigue & Fracture of Engineering Materials & Structures, 2020, 43(8): 1824–1836
39. Hashin Z, Rotem A. A cumulative damage theory of fatigue failure. Materials Science and Engineering, 1978, 34(2): 147–160
40. Jin R C, Chen W, Simpson T W. Comparative studies of metamodelling techniques under multiple modelling criteria. Structural and Multidisciplinary Optimization, 2001, 23(1): 1–13
41. Zhang J, Chowdhury S, Messac A. An adaptive hybrid surrogate model. Structural and Multidisciplinary Optimization, 2012, 46(2): 223–238
42. Karve P M, Guo Y L, Kapusuzoglu B, Mahadevan S, Haile M A. Digital twin approach for damage-tolerant mission planning under uncertainty. Engineering Fracture Mechanics, 2020, 225: 106766
43. Wojciechowski S, Maruda R W, Krolczyk G M, Niesłony P. Application of signal to noise ratio and grey relational analysis to minimize forces and vibrations during precise ball end milling. Precision Engineering, 2018, 51: 582–596